



Final Draft **of the original manuscript**

Thiangviriya, S.; Sitthiwet, C.; Plerdsranoy, P.; Capurso, G.; Pistidda, C.; Utke, O.; Dornheim, M.; Klassen, T.; Utke, R.:

Hydrogen sorption kinetics, hydrogen permeability, and thermal properties of compacted 2LiBH_4 single bond MgH_2 doped with activated carbon nanofibers.

In: International Journal of Hydrogen Energy. Vol. 44 (2019) 29, 15218 - 15227.

First published online by Elsevier: 15.05.2019

<https://dx.doi.org/10.1016/j.ijhydene.2019.04.146>

1 **Hydrogen sorption kinetics, hydrogen permeability, and thermal properties of**
2 **compacted 2LiBH₄-MgH₂ doped with activated carbon nanofibers**

3
4 Sophida Thiangviriyaya¹, Chongsutthamani Sitthiwet¹, Praphatsorn Plerdsranoy¹, Giovanni
5 Capurso², Claudio Pistidda², Oliver Utke³, Martin Dornheim², Thomas Klassen², Rapee
6 Utke^{1, 4, 5, *}

7
8 ¹School of Chemistry, Institute of Science, Suranaree University of Technology, Nakhon
9 Ratchasima 30000, Thailand.

10 ²Institute of Materials Research, Helmholtz-Zentrum Geesthacht, Max-Planck-Strasse 1, D-
11 21502 Geesthacht, Germany.

12 ³Mechanical System Division, Synchrotron Light Research Institute (Public Organization),
13 Nakhon Ratchasima 30000, Thailand.

14 ⁴Center of Excellence on Advanced Functional Materials (CoE-AFM), Suranaree University of
15 Technology, Nakhon Ratchasima 30000, Thailand.

16 ⁵NANOTEC-SUT Center of Excellence on Advanced Functional Nanomaterials, Suranaree
17 University of Technology, Thailand.

18
19 To improve the packing efficiency in tank scale, hydrides have been compacted into pellet
20 form; however, poor hydrogen permeability through the pellets results in sluggish kinetics.
21 In this work, the hydrogen sorption properties of compacted 2LiBH₄-MgH₂ doped with 30
22 wt. % activated carbon nanofibers (ACNF) are investigated. After doping with ACNF, onset
23 dehydrogenation temperature of compacted 2LiBH₄-MgH₂ decreases from 350 to 300 °C and
24 hydrogen released content enhances from 55 to 87 % of the theoretical capacity.
25 Furthermore, the sample containing ACNF releases hydrogen following a two-step
26 mechanism with reversible hydrogen storage capacities up to 4.5 wt. % H₂ and 41.8 gH₂/ L,
27 whereas the sample without ACNF shows a single-step decomposition mainly from MgH₂
28 with only 1.8 wt. % H₂ and 15.4 gH₂/L. Significant kinetic improvement observed in the

1 doped system appears due to the enhancement of both hydrogen permeability and heat
2 transfer through the pellet.

3

4 **Keywords:** Metal hydrides, carbon, hydrogen storage, dehydrogenation, reversibility.

5 * Corresponding author

6

7 **1. Introduction**

8 Lithium borohydride (LiBH_4) has attracted considerable attention due to its high
9 theoretical volumetric and gravimetric capacities of $121 \text{ kgH}_2/\text{m}^3$ and 18.5 wt. % H_2 ,
10 respectively [1-3]. However, high dehydrogenation temperature ($T > 400 \text{ }^\circ\text{C}$), sluggish
11 kinetics, severe hydrogenation conditions ($T = 600 \text{ }^\circ\text{C}$ and $p(\text{H}_2) = 350 \text{ bar}$), and poor
12 reversibility hinder its practical use [4]. Among several approaches, the reactive hydride
13 composites (RHCs) of LiBH_4 with other hydrides, such as $\text{LiBH}_4\text{-AlH}_3$ [5], $\text{Mg}_2\text{FeH}_6\text{-LiBH}_4$
14 [6], $\text{LiNH}_2\text{-MgH}_2\text{-LiBH}_4$ [7], and especially $\text{LiBH}_4\text{-MgH}_2$ [8-10] have been widely proposed.
15 During dehydrogenation of $2\text{LiBH}_4\text{-MgH}_2$, the formation of MgB_2 leads to the reduction of
16 dehydrogenation enthalpy by 25 kJ/mol H_2 with theoretical storage capacity of 11.4 wt. % H_2
17 [11]. However, its long incubation period of MgB_2 formation ($\sim 15 \text{ h}$) resulted in slow
18 kinetics, for example, up to 25 h to complete desorption [8]. By doping $2\text{LiBH}_4\text{-MgH}_2$ with
19 catalysts and additives of transition metal compounds, e.g., MoS_2 , CoNiB , halides (NbF_5 ,
20 TiF_3 , CeF_3 , LaF_3 , FeF_3 , TiCl_3 , CeCl_3 , VCl_3 , and CuCl_2), CeH_2 , SiO_2 , and titanium
21 isopropoxide (Tiso) [8, 12-16], substantial kinetic improvement was observed. For example,
22 onset dehydrogenation temperature of $2\text{LiBH}_4\text{-MgH}_2$ decreased from 350 to $\sim 200 \text{ }^\circ\text{C}$ after
23 doping with 20 wt. % MoS_2 [13] and incubation period disappeared by doing with NbF_5 and
24 Tiso [8, 14]. Besides transition metal-based compounds, carbon materials have been widely
25 used to develop de/rehydrogenation performance of hydrides. Introduction of carbon

1 fragments in hydride phase not only leads to fast hydrogen diffusion and thermal
2 conductivity, benefiting hydrogen ab/desorption kinetics, but also prevents particle
3 agglomeration during cycling [17-19]. Incubation period of $2\text{LiBH}_4\text{-MgH}_2$ was significantly
4 reduced by doping with 10 wt. % graphitic carbon nitride (C_3N_4); however, capacity loss up
5 to 1.5 wt. % H_2 during cycling was observed due to irreversible reaction of C_3N_4 and MgH_2
6 [20].

7 An approach pursued to enhance material packing efficiency, thermal conductivity,
8 and morphological stability during cycling is the compaction of the hydrogen storage material
9 in form of pellets [21-22]. However, high compaction pressure could degrade hydrogen
10 permeability through the compacted hydride, resulting in poor kinetics [21]. Compacted
11 MgH_2 doped with 10 wt. % expanded natural graphite (ENG) showed good thermal
12 conductivity and hydrogen permeability in the radial direction of the pellet [23]. Compacted
13 LiBH_4 nanoconfined in activated carbon nanofibers (ACNF) impregnated with TiO_2 revealed
14 superior hydrogen permeability in the axial direction, whereas compacted LiBH_4 showed no
15 sign of hydrogen permeability [24]. Woven fibrous structure of ACNF appeared both to
16 benefit hydrogen permeability and reinforce the pellet structure, yielding to good mechanical
17 stability during cycling [24-25]. Although kinetic improvement can be achieved significantly
18 by material confinement, hydrogen capacity is significantly lowered due to the weight of
19 carbon host. Recently, dehydrogenation kinetics of $2\text{LiBH}_4\text{-MgH}_2$ in loose powder form was
20 enhanced by doping with 1-30 wt. % ACNF [26]. Due to good hydrogen diffusion and heat
21 transport within ACNF, reduction of dehydrogenation temperature and fast hydrogen sorption
22 kinetics were obtained with increased ACNF content.

23 In the present work, a thorough study of the hydrogen sorption properties as well as
24 the materials features, such as hydrogen permeability and thermal properties of compacted
25 $2\text{LiBH}_4\text{-MgH}_2$ doped with 30 wt. % ACNF is reported. The choice of investigating this

1 specific system is due to its excellent performance in the loose powder form [26].
2 Compacted samples of $2\text{LiBH}_4\text{-MgH}_2$ with and without ACNF, owning the pellet densities of
3 $\sim 0.8\text{-}1.0\text{ g/cm}^3$ are prepared. De/rehydrogenation kinetics and reaction mechanisms of
4 compacted samples are investigated. Mechanical stability upon cycling, hydrogen
5 permeability, and thermal conductivity are also characterized.

6

7 **2. Experimental details**

8 Activated carbon nanofibers (ACNF) were prepared by activation of polyacrylonitrile
9 (PAN)-based electrospun nanofibers [27-28]. PAN ($M_w = 150,000\text{ g/mol}$, Sigma-Aldrich)
10 was dissolved in *N,N*-dimethylformamide (DMF, Carlo Erba Reagent) and stirred at room
11 temperature overnight to obtain a 10 %w/v solution. Electrospinning conditions including
12 solution flow rate, applied voltage, tip-to-collector distance, and temperature were 1.5 mL/h,
13 10 kV, 15 cm, and 35 °C, respectively. The obtained PAN nanofibers were stabilized in air at
14 280 °C for 3h and subsequently carbonized in N_2 at 1000 °C for 1 h to obtain carbon
15 nanofibers (CNFs). CNFs were activated by soaking in concentrated KOH solution (30%
16 w/v) for 2 h at 80 °C, drying at room temperature for 24 h, and heating at 800 °C under N_2
17 atmosphere for 15 min to obtain activated carbon nanofibers (ACNFs). Neutralization of
18 ACNFs was done by immersing in 0.5 M HCl solution at room temperature for 30 min and
19 washing with deionized water until neutral pH was reached. The obtained ACNFs were dried
20 at 120 °C for 24 h and treated at 500 °C under vacuum for 3 h. The powder samples of
21 LiBH_4 ($\geq 90\%$, hydrogen storage grade, Sigma-Aldrich) and powder Mg ($\geq 99\%$, Sigma-
22 Aldrich) were milled under 2:1 molar ratio ($\text{LiBH}_4\text{:MgH}_2$) in a stainless-steel vial by using a
23 SPEC Sample Prep 8000D DUAL Mixer/Mill. Ball-to-powder weight ratio (BPR) and
24 milling time were 10-20:1 and 5-10 h, respectively. The mixture was hydrogenated at 350 °C
25 under 80 bar H_2 for 12 h to obtain $2\text{LiBH}_4\text{-MgH}_2$ composite. ACNFs (30 wt. %) were doped

1 into 2LiBH₄-MgH₂ by ball milling technique with BPR and milling time of 10:1 and 30 min,
2 respectively, to obtain 2LiBH₄-MgH₂-30 %ACNFs. Loose powder samples (58-60 mg) of
3 2LiBH₄-MgH₂ and 2LiBH₄-MgH₂-30 %ACNFs were pressed into the pellets by using a
4 uniaxial laboratory hydraulic press with compaction pressure of 600 MPa on 12- to 13-mm
5 diameter die sets to obtain compacted samples, denoted as 2Li-MH and 2Li-MH-ACNF,
6 respectively.

7 Dehydrogenation profiles of compacted samples were investigated by simultaneous
8 differential scanning calorimetry (DSC)-thermogravimetry (TG) using a Netzsch STA 449 F3
9 Jupiter. Compacted samples (10-20 mg) were heated from room temperature to 500 °C (5
10 °C/min) under N₂ flow of 50 mL/min. Relative contents of hydrogen (H₂) and diborane
11 (B₂H₆) gases released upon heating were simultaneously monitored by mass spectroscopy
12 (MS) using a Netzsch QMS 403C mass spectrometer. Activation energy (E_A) for the
13 dehydrogenation process was characterized by DSC technique using a Netzsch 204 F1
14 PHOENIX. Compacted samples (~10 mg) were heated from room temperature to 500 °C
15 with heating rates of 5-20 °C/min under N₂ flow of 50 mL/min. According to the Kissinger
16 method (equation (1)), E_A was calculated from the slope of the plot between $\ln(\beta/T_p^2)$ and
17 $1/T_p$.

$$18 \ln(\beta/T_p^2) = -(E_A/RT_p) + \ln(k_0R/E_A) \quad (1)$$

19 where β and T_p are heating rate (5-20 °C/min) and peak temperature of dehydrogenation (K),
20 respectively. R and k_0 are gas constant (8.314 J K⁻¹ mol⁻¹) and frequency factor, respectively.

21 Dehydrogenation kinetics and reversibility of compacted samples were measured by
22 using a Sievert-type apparatus [29-31]. Compact sample (~60-70 mg) was packed into a
23 stainless-steel sample holder (SS316) under N₂ atmosphere in the glove box and transferred

1 to the Sievert-type apparatus. Two K-type thermocouples (-250 to 1300 °C, SL heater) were
2 attached to the sample holder and the furnace for measuring temperatures. Pressure
3 transducers (C206, Cole Parmer) with operating ranges of 0-500 and 0-3000 Psig were used
4 to measure the pressure changes during hydrogen desorption and absorption, respectively.
5 Thermocouples and pressure transducers were connected to an AI210I module convertor data
6 logger (Wisco), measuring and transferring (every 1 s) the pressure and temperature changes
7 to the computer. Dehydrogenation was carried out by heating the sample to 400 °C under 3
8 bar H₂ and rehydrogenation was performed at 400 °C under 80 bar H₂ for 12 h. Released
9 hydrogen content was calculated from the pressure change (Δp) and equations (2) and (3):

$$10 \quad (\Delta p)V = nRT \quad (2)$$

$$11 \quad \text{H}_2 \text{ desorbed (wt. \%)} = [(n \times 2.0158)/\text{sample weight}] \times 100 \quad (3)$$

12 where p , V , n , R , and T are hydrogen pressure (atm), system volume (L), moles of hydrogen
13 (mol), gas constant (0.0821 L atm K⁻¹ mol⁻¹), and temperature (K), respectively.

14 Powder x-ray diffraction (PXD) experiments were carried out by using a Bruker D2
15 PHASER with a Cu K_α radiation ($\lambda=1.5406 \text{ \AA}$). The samples were packed into an airtight
16 sample holder to prevent the material from being exposed to air and moisture. The
17 diffraction patterns were collected in a 2θ range of 10-80° with a scanning step of 0.02 °/s.
18 Fourier transform infrared spectroscopy (FTIR) spectra were collected by using a Bruker
19 Tensor 27-Hyperion 2000. Anhydrous KBr was ground with the sample in the mortar and
20 pressed to obtain KBr pellet. The spectra were recorded in the wavenumber range of 400-
21 4000 cm⁻¹ with 64 scans for both sample and background.

22 Anisotropic hydrogen permeability in the axial direction of compacted sample was
23 investigated by using a transient method reported in the previous works [24, 32]. Compacted

1 sample was tightly placed between two stainless-steel meshes (SS316, Swagelok) by using
 2 rubber O-rings. Two hydrogen permeability experiments were carried out at ambient
 3 temperature (~ 30 °C) by applying hydrogen pressure of ~ 0.65 MPa to the upstream chamber
 4 and evacuating the downstream chamber to ~ 0.07 MPa. The pressures of upstream and
 5 downstream chambers (P_u and P_d , respectively) were recorded by using pressure transducers
 6 (0-500 Psig, C206 Cole Parmer). The pressure degradation curve across the sample was
 7 explained as in equation (4).

$$8 \quad \frac{(P_u - P_d)}{(P_{u,0} - P_{d,0})} = e^{-\alpha t} \quad (4)$$

9 where $(P_u - P_d)$ and $(P_{u,0} - P_{d,0})$ are the pressure differences between upstream and downstream
 10 chambers (Pa) at specific time during the experiment and at the initial state, respectively. t is
 11 time (s) and α is described by equation (5).

$$12 \quad \alpha = \frac{kA(P_{u,0} + P_{d,0})}{2\mu L} \left(\frac{1}{V_u} + \frac{1}{V_d} \right) \quad (5)$$

13 where k is the hydrogen permeability (m^2), L is the sample thickness (0.55-0.60 mm), A is the
 14 sample cross-section area ($1.13 \times 10^{-4} \text{ m}^2$), μ is the hydrogen gas viscosity at 30 °C ($8.95 \times$
 15 10^{-6} Pa s) [33-34], and V_u and V_d are the volumes of upstream and downstream chambers,
 16 respectively (2.27×10^{-5} and $2.22 \times 10^{-5} \text{ m}^3$, respectively).

17 The thermal properties of compacted samples were characterized by a Transient Plane
 18 Source (TPS) method [35-36] using a TPS 1500 system (C3 Prozeß und Analysetechnik,
 19 Germany) with a sensor of 3.2 mm in radius. To enhance the contact between compacted
 20 sample and TPS sensor, a load of 2 kg was applied to keep the thin Kapton-insulated sensor
 21 firmly placed between two pellets. The measurements were performed at room temperature
 22 (~ 25 °C) with an input power of 200 mW and a measurement time of 20 s. All preparation

1 procedures and measurements were carried out under Ar atmosphere in the glove box to
2 avoid oxygen and humidity.

3

4 **3. Results and discussion**

5 The dehydrogenation profiles of 2Li-MH and 2Li-MH-ACNF are characterized by
6 simultaneous DSC-TG-MS measurements. From Figures 1 (A) and (B), DSC curves of 2Li-
7 MH and 2Li-MH-ACNF show endothermic peaks at 117-120.6 and 286-288.2 °C for phase
8 transformation of LiBH_4 (*o*- to *h*- LiBH_4) and melting of *h*- LiBH_4 , respectively.
9 Dehydrogenation of MgH_2 and LiBH_4 of 2Li-MH are at 369.7 and 442.0 °C, respectively,
10 while those of 2Li-MH-ACNF are at lower temperatures of 325.0 and 426.5 °C, respectively.
11 Moreover, onset dehydrogenation temperature of 2Li-MH reduces from about 350 to 300 °C
12 after doping with 30 wt. % ACNF. From TG and MS plots in Figure 1 (A), hydrogen content
13 released from 2Li-MH is 6.3 wt. % H_2 , in agreement with only 55 % of theoretical hydrogen
14 capacity of $2\text{LiBH}_4\text{-MgH}_2$ composite (11.4 wt. % H_2). By doping with 30 wt. % ACNF, the
15 theoretical capacity of 2Li-MH-ACNF is 7.98 wt. % H_2 . From Figure 1 (B), 6.95 wt. % H_2
16 (87 % of theoretical capacity) liberate from 2Li-MH-ACNF. In addition, dehydrogenation
17 kinetics and reversibility of compacted samples are investigated by volumetric method. From
18 Figure 2, 2Li-MH shows reversible single-step dehydrogenation with identical hydrogen
19 contents during the 1st and 2nd cycles of 1.8 wt. % H_2 . Considering simultaneous DSC-TG-
20 MS results (Figure 1 (A)), at 400 °C hydrogen desorbed from 2Li-MH is mainly from MgH_2
21 and only slightly from LiBH_4 . This is further supported by PXD and FTIR results (Figure 4).
22 For 2Li-MH-ACNF, two-step decomposition is observed for both the 1st and 2nd cycles with
23 greater hydrogen contents of 4.0-4.5 wt. % H_2 (Figure 2). Considering pellet volumes and
24 weights of 2Li-MH (0.070 cm^3 and 0.060 g, respectively) and 2Li-MH-ACNF (0.062 cm^3

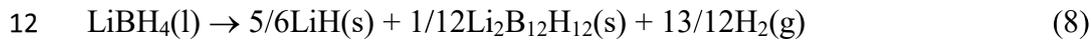
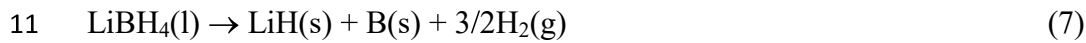
1 and 0.057 g, respectively), volumetric hydrogen capacities of 2Li-MH and 2Li-MH-ACNF
2 are 15.4 and 41.8 gH₂/L, respectively. Significant kinetic improvement of 2Li-MH after
3 doping with 30 wt. % ACNF might be related to the enhanced hydrogen permeability and
4 thermal properties, further discussed in Figure 6 and Table 2. The amount of hydrogen
5 released in the first step, corresponding to the decomposition of MgH₂ reduces upon cycling
6 from ~2.0 and 1.0 wt. % H₂ for the 1st and 2nd cycles, respectively (Figure 2). It should be
7 noted that incubation period during the 2nd dehydrogenation of 2Li-MH-ACNF (~1 h) is
8 significantly shorter than that of the 1st one (~6 h) (Figure 2). For example, LiBH₄ starts to
9 decompose at ~7-8 h during the 1st cycle, while that of the 2nd cycle is at ~3 h. Upon cycling,
10 the formation of cracks and/or defects can occur due to pellet expansion/contraction during
11 hydrogen ab/desorption. Thus, hydrogen permeability through the pellet might be improved,
12 benefitting hydrogen sorption kinetics [21].

13 The activation energy (E_A) for dehydrogenation of 2Li-MH and 2Li-MH-ACNF was
14 investigated by DSC technique. From Figures 3 (A) and (C), DSC curves with heating rates
15 of 5-20 °C/min show endothermic peaks corresponding to *h*-LiBH₄ melting at 288-297 °C
16 and to dehydrogenation of MgH₂ and LiBH₄ at 339-395.2 and 402-497 °C, respectively. Two
17 endothermic peaks detected during dehydrogenation of LiBH₄ are denoted as the 1st- and 2nd-
18 LiBH₄, representing the peaks at low and high temperatures, respectively. By using
19 Kissinger equation (equation (1)), E_A of each dehydrogenation step can be calculated from
20 the slope of the Kissinger plots ($\ln(\beta/T_p^2)$ versus $1/T_p$). The calculated E_A of 2Li-MH for
21 dehydrogenation of MgH₂, 1st-LiBH₄, and 2nd-LiBH₄ are 245, 130, and 143.4 kJ/mol H₂,
22 respectively, while those of 2Li-MH-ACNF decrease to 178, 104.3, and 135 kJ/mol,
23 respectively (Figures 3 (B) and (D)). Significant reduction of E_A of compacted sample after
24 doping with 30 wt. % ACNF (ΔE_A = up to 67 kJ/mol for MgH₂ decomposition) hints at

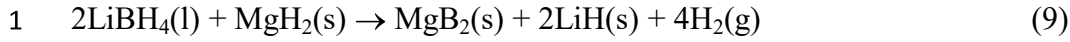
1 kinetic improvement, in agreement with titration results (Figure 2). Another important issue
2 of compacted hydride is mechanical stability since large strain changes upon
3 de/rehydrogenation cycles yield to the decrepitation and disaggregation of compacted sample
4 [37]. Unexpected volumetric contraction/expansion lead to stress and deformation of the
5 container wall [38]. From Table 1, as-prepared pellets of 2Li-MH and 2Li-MH-ACNF have
6 regular shape after compaction with pellet densities of ~ 0.86 and 0.93 g/cm^3 , respectively.
7 The increment of pellet density indicates the improvement of compaction after doping with
8 ACNF probably owing to the lubrication effect of ACNF for compaction as ENG doped into
9 compacted hydride [39]. After rehydrogenation, 2Li-MH cannot preserve its pellet shape and
10 turns completely to loose powder form, whereas 2Li-MH-ACNF maintains its shape with
11 small crack (Table 1). Superior mechanical stability can be described by the fact that the
12 fibrous structure of ACNF probably plays an important role as reinforced frameworks for
13 compacted sample [25].

14 Furthermore, reaction mechanisms during de/rehydrogenation of 2Li-MH and 2Li-
15 MH-ACNF are studied by PXD and FTIR techniques. From Figure 4 (A) (a), as-prepared
16 pellet of 2Li-MH reveals diffraction patterns of LiBH_4 , hydrated LiBH_4 [40], and MgH_2 ,
17 suggesting no reactions occurring during sample preparation. Hydrated LiBH_4 is formed by
18 the introduction of structural water into LiBH_4 lattice without side reactions, leading to
19 hydrogen desorption [40]. After dehydrogenation ($T=400 \text{ }^\circ\text{C}$ and $p(\text{H}_2)=3 \text{ bar}$), the signals of
20 Mg and LiH are observed, implying individual dehydrogenation of MgH_2 (equation (6)) and
21 LiBH_4 (equations (7) and (8)), respectively) (Figure 4 (A) (b)). Moreover, the residual LiBH_4
22 suggests incomplete dehydrogenation of 2Li-MH, corresponding to deficient hydrogen
23 content released during titration measurements (Figure 2). MgO is due to oxidation of Mg-
24 containing phases during the experiments. In the case of rehydrogenated pellet ($T=400 \text{ }^\circ\text{C}$
25 and $p(\text{H}_2)=80 \text{ bar}$), reversibility of MgH_2 is detected with unreacted LiBH_4 and MgO (Figure

1 4 (A) (c)). The disappearance of LiH also implies reversibility of LiBH₄. Besides, B-
 2 containing phases formed during de/rehydrogenation are characterized by FTIR technique.
 3 From Figure 4 (B), all samples show strong vibrational peaks of B-H stretching and bending
 4 of LiBH₄ at 2388-2224 and 1124 cm⁻¹, respectively [28, 41], together with O-H bending of
 5 oxygen and humidity during experiments at 1637 cm⁻¹ [30]. Dehydrogenated and
 6 rehydrogenated pellets display [B₁₂H₁₂]²⁻ vibration of Li₂B₁₂H₁₂ at 2486 cm⁻¹ [42] and
 7 asymmetric B-O stretching due to oxidation of amorphous B (a-B) at 1600-1300 cm⁻¹ [43-
 8 44]. The formations of a-B and Li₂B₁₂H₁₂ confirm dehydrogenation of LiBH₄ according to
 9 equations (7) and (8).



13 For 2Li-MH-AC, as-prepared pellet shows diffraction peaks of LiBH₄, hydrated
 14 LiBH₄, and MgH₂ (Figure 5 (A) (a)), indicating no reactions occurring during sample
 15 preparation. After dehydrogenation, the signals of MgB₂, Mg, and LiH are observed together
 16 with a trace of incomplete dehydrogenated MgH₂ (Figure 5 (A) (b)). The formation of MgB₂
 17 indicates dehydrogenation of LiBH₄ and MgH₂ according to equation (9) and agrees with
 18 two-step decomposition observed in titration results (Figure 2). For rehydrogenated pellet,
 19 diffraction peaks of MgH₂, MgO, and unknown phase are detected (Figure 5 (A) (c)).
 20 Disappearance of LiBH₄ diffraction can be due to amorphous and/or nanosized particles.
 21 Significant amount of MgO obtained after rehydrogenation leads to reduction of hydrogen
 22 content released from decomposition of MgH₂ during the 2nd cycle as shown in titration result
 23 in Figure 2.



2 For FTIR results, vibrational peaks of B-H stretching ($2392\text{-}2224 \text{ cm}^{-1}$) and bending (1128
3 cm^{-1}) of LiBH_4 and O-H bending (1636 cm^{-1}) of oxygen and/or humidity during the
4 experiments are found in all pellets (Figure 5 (B)). Dehydrogenated pellet reveals vibrational
5 peaks of $[\text{B}_{12}\text{H}_{12}]^{2-}$ at 2486 cm^{-1} and asymmetric B-O stretching at $1600\text{-}1300 \text{ cm}^{-1}$ from
6 $\text{Li}_2\text{B}_{12}\text{H}_{12}$ and oxidation of a-B, respectively (Figure 5 (B) (b)), hinting at individual
7 dehydrogenation of LiBH_4 according to equations (7) and (8). Residual LiBH_4 implies
8 incomplete dehydrogenation, in accordance with deficient hydrogen content released with
9 respect to theoretical capacity (Figure 2). After rehydrogenation (Figure 5 (B) (c)), the
10 enhanced signal of LiBH_4 suggests its reversibility; however, incomplete reaction is observed
11 by the vibrations of $\text{Li}_2\text{B}_{12}\text{H}_{12}$ (2486 cm^{-1}) and oxidation of a-B ($1500\text{-}1300 \text{ cm}^{-1}$),
12 corresponding to slight reduction of hydrogen content released during the 2nd cycle (Figure
13 2).

14 Hydrogen permeability in the axial direction of compacted samples was carried out by
15 using the setup calibrated and reported in the previous work [24]. From Figure 6 (A), 2Li-
16 MH shows gradual reduction of upstream pressure (P_u) together with increase of downstream
17 pressure (P_d) until identical pressure is reached at 15 h. For 2L-MH-ACNF, P_u and P_d
18 change rapidly and are comparable within 1 h. To investigate hydrogen permeability,
19 equation (4) is rearranged to obtain the linear correlation (equation (10)).

$$20 \quad \ln\left(\frac{(P_u - P_d)}{(P_{u,0} - P_{d,0})}\right) = -\alpha t \quad (10)$$

21 Hydrogen permeability (k) can be calculated as in equation (5) by using α obtained from the
22 slope of linear plot of $\ln[(P_u - P_d)/(P_{u,0} - P_{d,0})]$ versus t . From Figure 6 (B)), α and k of 2Li-MH
23 are $8.82 \times 10^{-5} \text{ s}^{-1} \pm 0.7 \%$ and $1.34 \times 10^{-19} \text{ m}^2 \pm 0.8 \%$, respectively, while those of 2Li-MH-

1 ACNF are $9.47 \times 10^{-4} \text{ s}^{-1} \pm 0.1 \%$ and $1.30 \times 10^{-18} \text{ m}^2 \pm 0.8 \%$, respectively. It should be noted
2 that hydrogen permeability in the axial direction of 2Li-MH enhances by an order of
3 magnitude after doping with 30 % ACNF. Regarding the previous studies [21, 23-24]
4 dehydrogenation kinetics was benefited by good hydrogen permeability. Thus, superior
5 hydrogen permeability of 2L-MH-ACNF to 2Li-MH lead to the improvement of kinetics, in
6 agreement with simultaneous DSC-TG-MS and titration measurements (Figures 1 and 2).
7 Moreover, it was reported that hydrogen back pressure of 3-5 bar encouraged simultaneous
8 desorption of LiBH_4 and formation of MgB_2 during dehydrogenation of $2\text{LiBH}_4\text{-MgH}_2$ at 400
9 °C without formation of intermediate metallic Mg [44]. Due to poor hydrogen permeability
10 of 2Li-MH, hydrogen pressure applied during dehydrogenation might not be able to reach the
11 sample bulk, especially at the center of the pellet, resulting in individual decomposition of
12 MgH_2 and LiBH_4 . For 2Li-MH-ACNF, superior hydrogen permeability promotes not only
13 dehydrogenation of LiBH_4 , but also formation of MgB_2 during dehydrogenation (equation (9)
14 and Figure 5 (A)). In addition, cracks and/or defects formed in 2Li-MH-ACNF upon cycling
15 enhancing hydrogen permeability yield to shorten incubation period during the 2nd
16 dehydrogenation (Figure 2).

17 Since de/rehydrogenation of hydride materials are endo-/exothermic reaction, heat
18 transfer inside the pellet is another important issue addressed to improve hydrogen exchange
19 rate. Table 2 shows comparable thermal conductivity of 2Li-MH and 2Li-MH-ACNF (1.6-
20 $1.67 \text{ W/mK} \pm 0.18 \%$). Thermal diffusivity and specific heat capacity of 2Li-MH are 0.20
21 $\text{mm}^2/\text{s} \pm 0.45 \%$ and $8.16 \text{ MJ/m}^3 \text{ K} \pm 0.37 \%$, respectively, while those of 2Li-MH-ACNF are
22 $0.33 \text{ mm}^2/\text{s} \pm 0.88 \%$ and $5.04 \text{ MJ/m}^3 \text{ K} \pm 0.70 \%$, respectively (Table 2). From the previous
23 work, introduction of carbon material with elongated shape (e.g., ENG) significantly
24 increased anisotropy of thermal conductivity (along ENG alignment) [23]. However, in our
25 case isotropic thermal conductivity is presumedly achieved from 2Li-MH-ACNF because the

1 milling procedure could homogenize shape and distribution of the ACNF in hydride matrices.
2 Considering the equation $\alpha = k / \rho C_p$, where α , k , ρ , and C_p are thermal diffusivity, thermal
3 conductivity, mass density, and specific heat capacity, respectively [36], thermal diffusivity is
4 the ratio of heat conduction to heat storage. The higher the thermal diffusivity, the faster the
5 propagation of heat into the compacted sample. Thus, the higher thermal diffusivity and
6 lower specific heat capacity of 2Li-MH-ACNF with respect to 2Li-MH suggest its enhanced
7 heat transfer properties. Since thermal conductivities of 2Li-MH and 2Li-MH-ACNF are
8 comparable with slight increment of pellet density after ACNF doping (0.86 to 0.93 g/cm³),
9 improved heat transfer of 2Li-MH-ACNF is likely to be due to the addition of ACNF. Owing
10 to the improvement of hydrogen diffusion and heat transfer of compacted 2LiBH₄-MgH₂ after
11 doping with ACNF, faster kinetics and effective reversibility are obtained. Moreover, fibrous
12 structure of ACNF probably acts as reinforced framework, yielding to mechanical stability of
13 compacted hydride upon cycling.

14

15 **4. Conclusions**

16 Hydrogen sorption kinetics, mechanical stability, hydrogen permeability, and heat transfer of
17 compacted 2LiBH₄-MgH₂ doped activated carbon nanofibers (ACNF) were investigated. By
18 doping with 30 wt. % ACNF, decomposition of both MgH₂ and LiBH₄ were accomplished,
19 leading to increase of gravimetric and volumetric reversible capacities from 1.8 to 4.5 wt. %
20 H₂ and from 15.4 to 41.8 gH₂/L, respectively. Hydrogen contents released and reproduced
21 from the samples with and without ACNF were deficient as compared with theoretical
22 capacity due to incomplete decomposition of LiBH₄ and the formation of thermally stable
23 phase of Li₂B₁₂H₁₂. Hydrogen permeability of compacted hydride with ACNF developed
24 upon cycling resulted in significantly shortened incubation period for MgB₂ formation from 6

1 to 1 h, while the sample without ACNF showed no improvement. Since fibrous structure of
2 ACNF could act as reinforced framework for compacted hydride, mechanical stability upon
3 cycling was accomplished. Activation energy (E_A) during dehydrogenation decreased after
4 doping ACNF into compacted hydride ($\Delta E_A =$ up to 67 kJ/mol). Hydrogen permeability in
5 the axial direction of compacted hydride with ACNF was an order of magnitude faster than
6 the one without ACNF. For thermal properties, ACNF favored heat transfer in the compacted
7 hydride confirmed as enhanced thermal diffusivity (from 0.2 to 0.33 mm²/s) and reduced
8 specific heat capacity (from 8.16 to 5.04 MJ/m³ K). Due to the improvement hydrogen
9 permeability and heat transfer after doping with ACNF, hydrogen sorption kinetics and
10 reversibility of compacted hydride were significantly developed.

11

12 **5. Acknowledgement**

13 The author would like to acknowledge The Thailand Research Fund and Suranaree
14 University of Technology (TRF Research Career Development Grant), The Royal Golden
15 Jubilee PhD. program (PHD/0153/2558), and Suranaree University of Technology (Full-time
16 61/10/2561) for financial support. This work has been partially supported by the Research
17 Network NANOTEC (RNN) program of the National Nanotechnology Center (NANOTEC),
18 NSTDA, Ministry of Science and Technology, Thailand.

19

20 **6. Table and Figure captions**

21 Table 1. Photographs of 2Li-MH and 2Li-MH-ACNF in as-prepared and rehydrogenated
22 states.

23 Table 2. Thermal properties of as-prepared pellets of 2Li-MH and 2Li-MH-ACNF.

1 Figure 1. Simultaneous DSC-TG-MS results during dehydrogenation of 2Li-MH (A) and 2Li-
2 MH-ACNF (B)

3 Figure 2. Dehydrogenation kinetics and reversibility of 2Li-MH and 2Li-MH-ACNF.

4 Figure 3. DSC curves with heating rates of 5-20 °C/min and the Kissinger plots of 2Li-MH
5 ((A) and (B), respectively) and 2Li-MH-ACNF ((C) and (D), respectively).

6 Figure 4. PXD (A) and FTIR (B) spectra of as-prepared (a), dehydrogenated (b), and
7 rehydrogenated (c) pellets of 2Li-MH.

8 Figure 5. PXD (A) and FTIR (B) spectra of as-prepared (a), dehydrogenated (b), and
9 rehydrogenated (c) pellets of 2Li-MH-ACNF.

10 Figure 6. P_u and P_d versus time (A) and hydrogen permeability (B) of 2Li-MH and 2Li-MH-
11 ACNF.

12

13 7. References

14 [1] Züttel A, Wenger P, Rentsch S, Sudan P, Mauron Ph, Emmenegger Ch. LiBH_4 a new
15 hydrogen storage material. J Power Sources 2003; 118: 1-7.

16 [2] Züttel A, Borgschulte A, Orimo SI. Tetrahydroborates as new hydrogen storage materials.
17 Scr Mater 2007; 56: 823-8.

18 [3] Puzkiel J, Garroni S, Milanese C, Gennari F, Klassen T, Dornheim M, et al.

19 Tetrahydroborates: Development and Potential as Hydrogen Storage Medium.

20 Inorganics 2017; 5: 74.

21 [4] Orimo S, Nakamori Y, Kitahara G, Miwa K, Ohba N, Towata S, et al. Dehydrogenating and
22 rehydrogenating reactions of LiBH_4 . J Alloys Compd 2005; 404-406: 427-30.

- 1 [5] Liu H, Wang X, Zhou H, Gao S, Ge H, Li S, et al. Improved hydrogen desorption
2 properties of LiBH₄ by AlH₃ addition. *Int J Hydrogen Energy* 2016; 41: 22118-27.
- 3 [6] Langmi HW, McGrady GS, Newhouse R, Rönnebro E. Mg₂FeH₆-LiBH₄ and Mg₂FeH₆-
4 LiNH₂ composite materials for hydrogen storage. *Int J Hydrogen Energy* 2012; 37:
5 6694-9.
- 6 [7] Zhang X, Li Z, Lv F, Li H, Mi J, Wang S, et al. Improved hydrogen storage performance
7 of the LiNH₂-MgH₂-LiBH₄ system by addition of ZrCo hydride. *Int J Hydrogen Energy*
8 2010; 35: 7809-14.
- 9 [8] Bösenberg U, Doppiu S, Mosegaard L, Barkhordarian G, Eigen N, Borgschulte A, et al.
10 Hydrogen sorption properties of MgH₂-LiBH₄ composites. *Acta Mater* 2007; 55: 3951-8.
- 11 [9] Jepsen J, Milanese C, Puzkiel J, Girella A, Schiavo B, Lozano GA, et al. Fundamental
12 Material Properties of the 2LiBH₄-MgH₂ Reactive Hydride Composite for Hydrogen
13 Storage: (I) Thermodynamic and Heat Transfer Properties. *Energies* 2018; 11: 1081.
- 14 [10] Jepsen J, Milanese C, Puzkiel J, Girella A, Schiavo B, Lozano GA, et al. Fundamental
15 Material Properties of the 2LiBH₄-MgH₂ Reactive Hydride Composite for Hydrogen
16 Storage: (II) Kinetic Properties. *Energies* 2018; 11: 1170.
- 17 [11] Vajo JJ, Skeith SL. Reversible Storage of Hydrogen in Destabilized LiBH₄. *J Phys*
18 *Chem B* 2005; 109: 3719-22.
- 19 [12] Zhao Y, Ding L, Zhong T, Yuan H, Jiao L. Hydrogen storage behavior of 2LiBH₄/MgH₂
20 composites improved by the catalysis of CoNiB nanoparticles. *Int J Hydrogen Energy*
21 2014; 39: 11055-60.
- 22 [13] Wang J, Han S, Zhang W, Liang D, Li Y, Zhao X, et al. Effects of MoS₂ addition on the
23 hydrogen storage properties of 2LiBH₄-MgH₂ systems. *Int J Hydrogen Energy* 2013; 38:
24 14631-7.

- 1 [14] Kou H, Xiao X, Li J, Li S, Ge H, Wang Q, et al. Effects of fluoride additives on
2 dehydrogenation behaviors of $2\text{LiBH}_4+\text{MgH}_2$ system. *Int J Hydrogen Energy* 2010; 37:
3 1021-6.
- 4 [15] Liu BH, Zhang BJ, Jiang Y. Hydrogen storage performance of $\text{LiBH}_4+1/2\text{MgH}_2$
5 composites improved by Ce-based additives. *Int J Hydrogen Energy* 2011; 36: 5418-24.
- 6 [16] Jiang Y, Liu BH. Dehydrogenation kinetics of $2\text{LiBH}_4+\text{MgH}_2$ enhanced by hydrogen
7 back pressure and a CuCl_2 catalyst. *J Alloys Compd* 2011; 509: 9055-9.
- 8 [17] Adelhelm P, de Jongh PE. The impact of carbon materials on the hydrogen storage
9 properties of light metal hydrides. *J Mater Chem* 2011; 21: 2417-27.
- 10 [18] Lillo-Ródenas MA, Guo ZX, Aguey-Zinsou KF, Cazorla- Amorós D, Linares-Solano A.
11 Effects of different carbon materials on MgH_2 decomposition. *Carbon* 2008; 46: 126-37.
- 12 [19] Awad AS, Nakhil M, Zakhour M, Santos SF, Souza FL, Bobet JL. Effect of microwave
13 irradiation on hydrogen sorption properties of hand mixed MgH_2 -10 wt.% carbon fibers.
14 *J Alloys Compd* 2016; 676: 1-8.
- 15 [20] Wang K, Kang X, Zhong Y, Hu C, Wang P. Improved reversible dehydrogenation
16 properties of $2\text{LiBH}_4\text{-MgH}_2$ composite by milling with graphitic carbon nitride. *Int J*
17 *Hydrogen Energy* 2014; 39: 13369-74.
- 18 [21] Jepsen J, Milanese C, Girella A, Lozano GA, Pistidda C, Bellosta von Colbe JM, et al.
19 Compaction pressure influence on material properties and sorption behaviour of $\text{LiBH}_4\text{-}$
20 MgH_2 composite. *Int J Hydrogen Energy* 2012; 38: 8357-66.
- 21 [22] Plerdsranoy P, Chanthee S, Utke R. Compaction of $\text{LiBH}_4\text{-MgH}_2$ doped with MWCNTs-
22 TiO_2 for reversible hydrogen storage. *Int J hydrogen Energy* 2017; 42: 978-86.
- 23 [23] Chaise A, de Rango P, Marty Ph, Fruchart D, Miraglia S, Olivès R, et al. Enhancement
24 of hydrogen sorption in magnesium hydride using expanded natural graphite. *Int J*
25 *Hydrogen Energy* 2009; 34: 8589-96.

- 1 [24] Sitthiwet C, Thiangviriyaya S, Thaweelap N, Meethom S, Kaewsuwan D, Chanlek N, et al.
2 Hydrogen sorption and permeability of compacted LiBH_4 nanoconfined into activated
3 carbon nanofibers impregnated with TiO_2 . *J Phys Chem Solids* 2017; 110: 344-53.
- 4 [25] Plerdsranoy P, Javadian P, Jensen ND, Nielsen UG, Jensen TR, Utke R. Compaction of
5 LiBH_4 - LiAlH_4 nanoconfined in activated carbon nanofibers: Dehydrogenation kinetics,
6 reversibility, and mechanical stability during cycling. *Int J Hydrogen Energy* 2017; 42:
7 1036-47.
- 8 [26] Thaingviriyaya S, Utke R. Improvement of dehydrogenation kinetics of 2LiBH_4 - MgH_2
9 composite by doping with activated carbon nanofibers. *Int J hydrogen Energy* 2016; 41:
10 2797-806.
- 11 [27] Lee HY, Kim HG, Kang SJ, Park SJ, An KH, Kim BJ. Effects of pore structures on
12 electrochemical behaviors of polyacrylonitrile (PAN)-based activated carbon nanofibers.
13 *J ind Eng Chem* 2014; 21: 736-40.
- 14 [28] Thiangviriyaya S, Utke R. LiBH_4 nanoconfined in activated carbon nanofiber for reversible
15 hydrogen storage. *Int J Hydrogen Energy* 2015; 40: 4167-74.
- 16 [29] Thaweelap N, Utke R. Dehydrogenation kinetics and reversibility of LiAlH_4 - LiBH_4
17 doped with Ti-based additives and MWCNT. *J Phys Chem Solids* 2016; 98: 149-55.
- 18 [30] Gosalawit-Utke R, Meethom S, Pistidda C, Milanese C, Laipple D, Saisopa T, et al.
19 Destabilization of LiBH_4 by nanoconfinement in PMMA-co-BM polymer matrix for
20 reversible hydrogen storage. *Int J. Hydrogen Energy* 2014; 39: 5019-29.
- 21 [31] Plerdsranoy P, Meethom S, Utke R. Dehydrogenation kinetics, reversibility, and reaction
22 mechanisms of reversible hydrogen storage material based on nanoconfined MgH_2 -
23 NaAlH_4 . *J Phys Chem Solids* 2015; 87: 16-22.
- 24 [32] Pan Z, Ma Y, Connel LD, Down DI, Camilleri M. Measuring anisotropic permeability
25 using a cubic shale sample in a triaxial cell. *J Nat Gas Sci Eng* 2015; 26: 336-44.

- 1 [33] <https://www.lmnoeng.com/Flow/GasViscosity.php>
- 2 [34] Flow of Fluids through Valves, Fittings, and Pipe, Crane Company, 1988. Technical
3 Paper No. 40 (TP 410).
- 4 [35] Gustafsson SE. Transient plane source techniques for thermal conductivity and thermal
5 diffusivity measurements of solid materials. Rev Sci Instrum 1991; 62: 797-804.
- 6 [36] Flueckiger S, Voskuilen T, Pourpoint T, Fisher TS, Zheng Y. In situ characterization of
7 metal hydride thermal transport properties. Int J Hydrogen Energy 2010; 35: 614–21.
- 8 [37] Kim KJ, Montoya B, Razani A, Lee KH. Metal hydride compacts of improved thermal
9 conductivity. Int J Hydrogen Energy 2001; 26: 609-13.
- 10 [38] Lozano GA, Bellosta von Colbe JM, Bormann R, Klassen T, Dornheim M. Enhanced
11 volumetric hydrogen density in sodium alanate by compaction. J Power Sources 2011;
12 196: 9254-9.
- 13 [39] Pohlmann C, Röntzsch L, Kalinichenka S, Hutsch T, Kieback B. Magnesium alloy-
14 graphite composites with tailored heat conduction properties for hydrogen storage
15 applications. Int J Hydrogen Energy 2010; 35: 12829-36.
- 16 [40] Takano A, Oikawa I, Kamegawa A, Takamura H. Enhancement of the lithium-ion
17 conductivity of LiBH_4 by hydration. Solid State Ionics 2016; 285: 47-50.
- 18 [41] Plerdsranoy P, Utke R. Confined LiBH_4 - LiAlH_4 in nanopores of activated carbon
19 nanofibers. Int J Hydrogen Energy 2015; 40: 7083-92.
- 20 [42] Huang Z, Gallucci J, Chen X, Yisgedu T, Lingam HK, Shore SG, et al. $\text{Li}_2\text{B}_{12}\text{H}_{12}\cdot 7\text{NH}_3$:
21 a new ammine complex for ammonia storage or indirect hydrogen storage. J Mater
22 Chem 2010; 20: 2743-5.
- 23 [43] Kamitsos EI, Karakassides MA, Chryssikos GD. Vibrational Spectra of Magnesium-
24 Sodium-Borate Glasses. 2. Raman and Mid-Infrared Investigation of the Network
25 Structure. J Phys Chem 1987, 91, 1073-9.

1 [44] Bösenberg U, Ravnsbæk DB, Hagemann H, D'Anna V, Bonatto Minella C, Pistidda C,
2 et al. Pressure and Temperature Influence on the Desorption Pathway of the LiBH₄-
3 MgH₂ Composite System. J Phys Chem C 2010; 114: 15212-7.

4

Table 1

Table 1

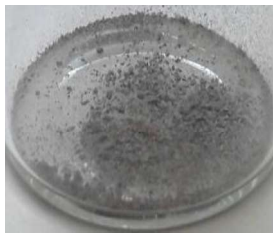
Compacted samples	As-prepared pellets	Rehydrogenated pellets
2Li-MH		
2Li-MH-ACNF		

Table 2

Table 2

Compacted samples	Thermal conductivity (W/mK)	Thermal diffusivity (mm ² /s)	Specific heat capacity (MJ/m ³ K)
2Li-MH	1.64±0.18 %	0.20±0.45%	8.16±0.37 %
2Li-MH-ACNF	1.67±0.18 %	0.33±0.88 %	5.04±0.70 %

Figure 1

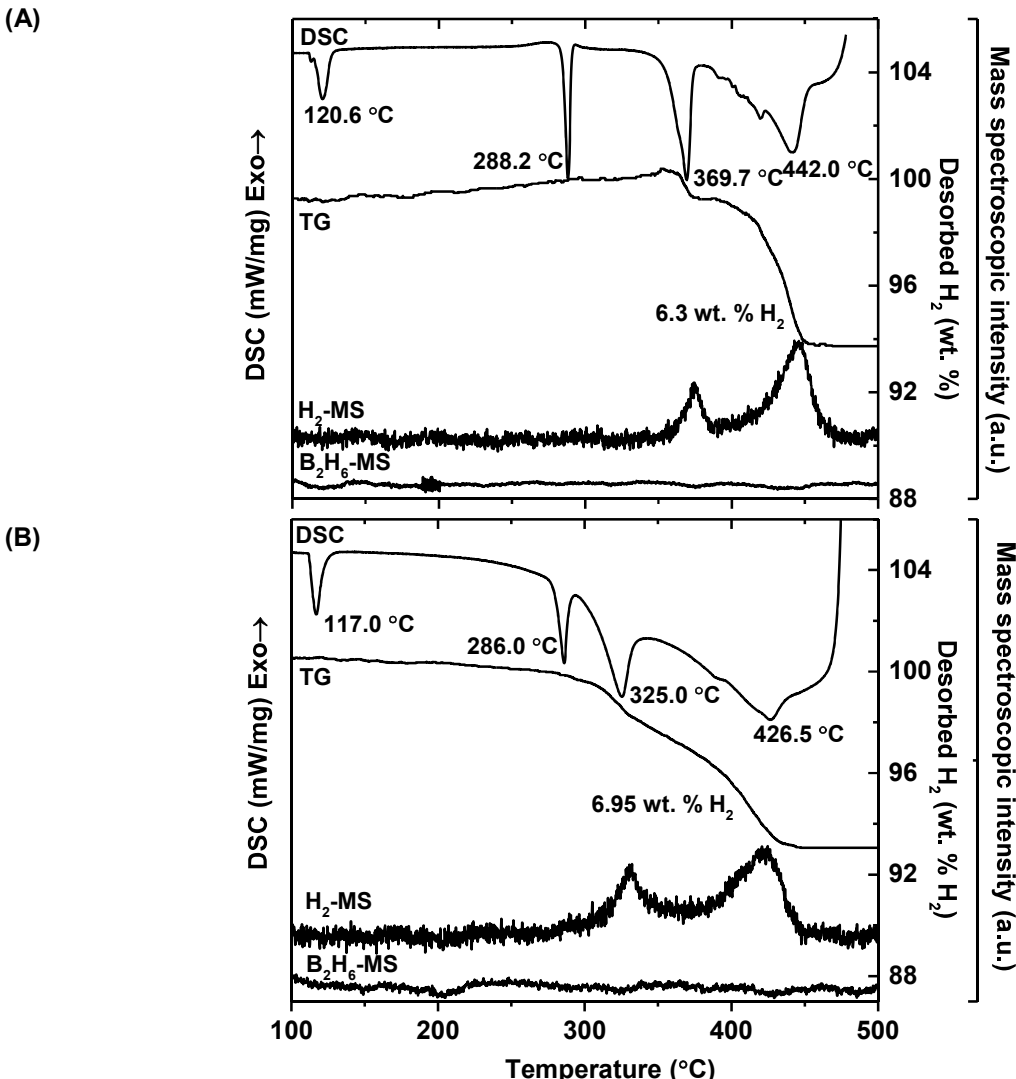


Figure 1

Figure 2

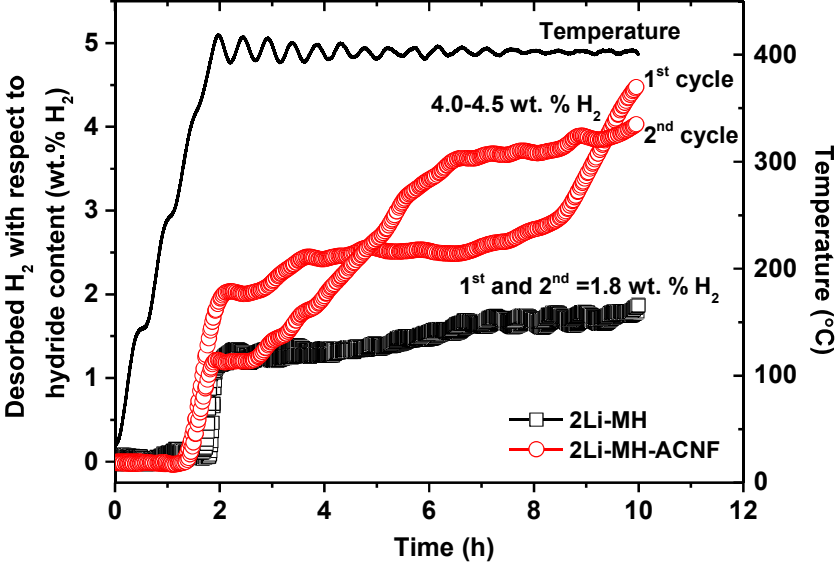


Figure 2

Figure 3

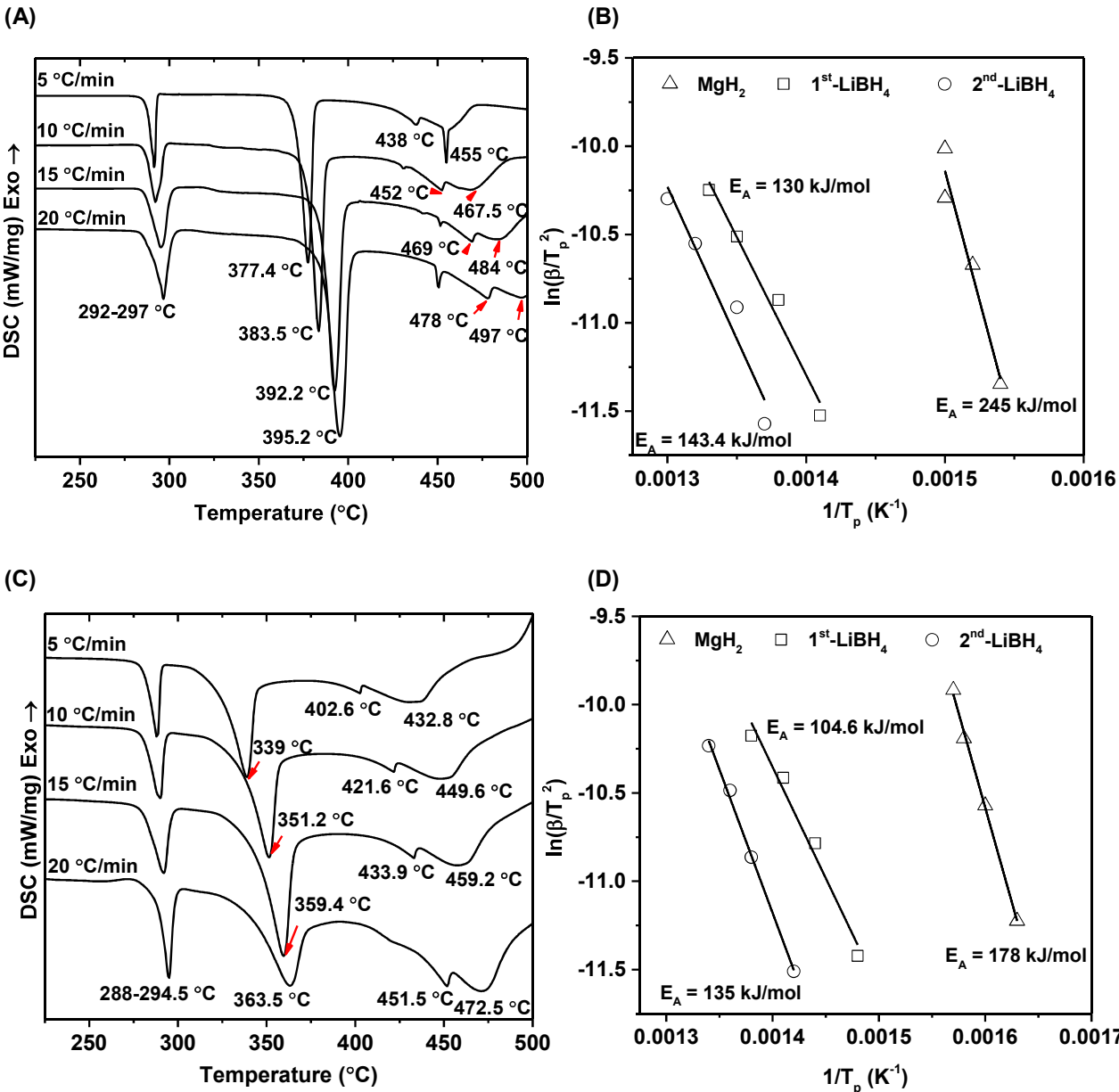


Figure 3

Figure 4

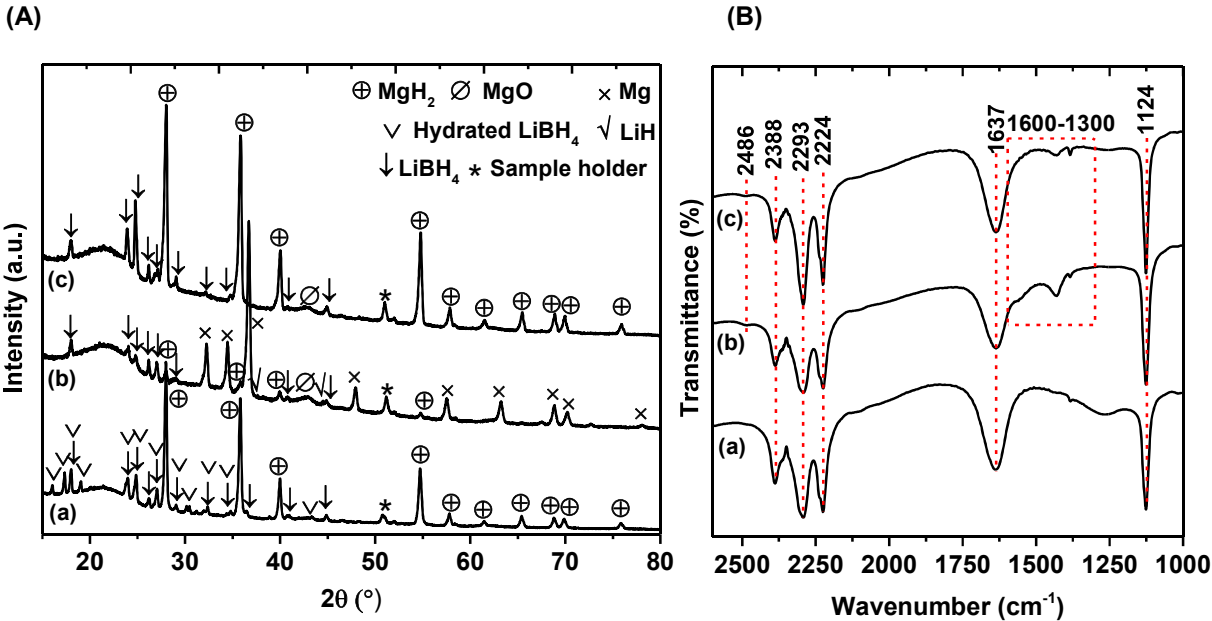


Figure 4

Figure 5

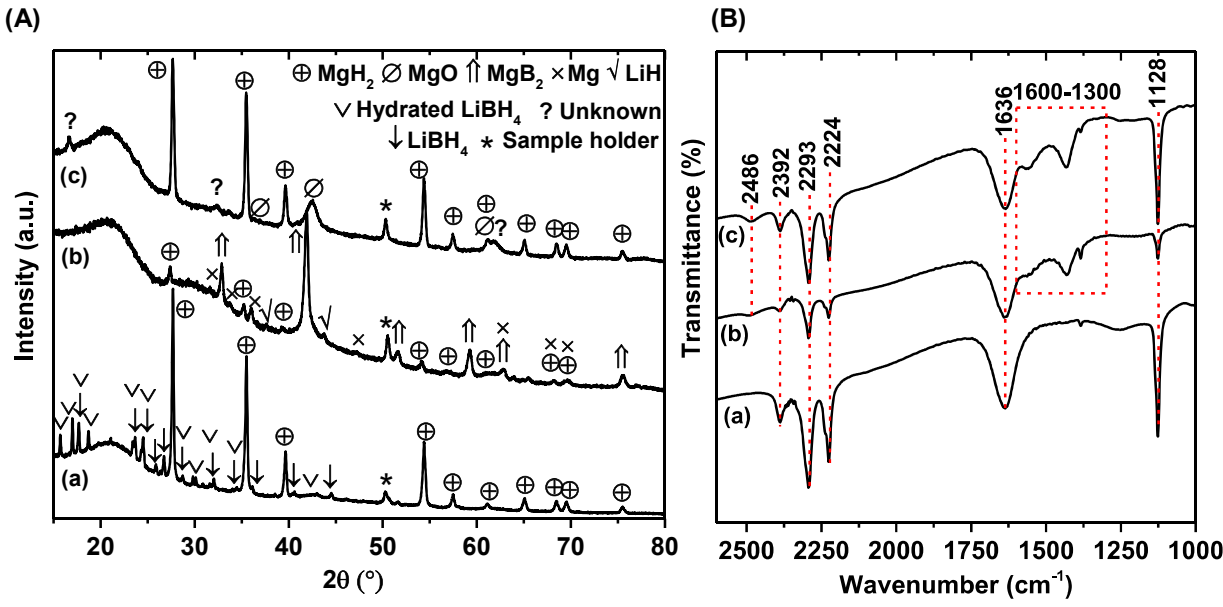
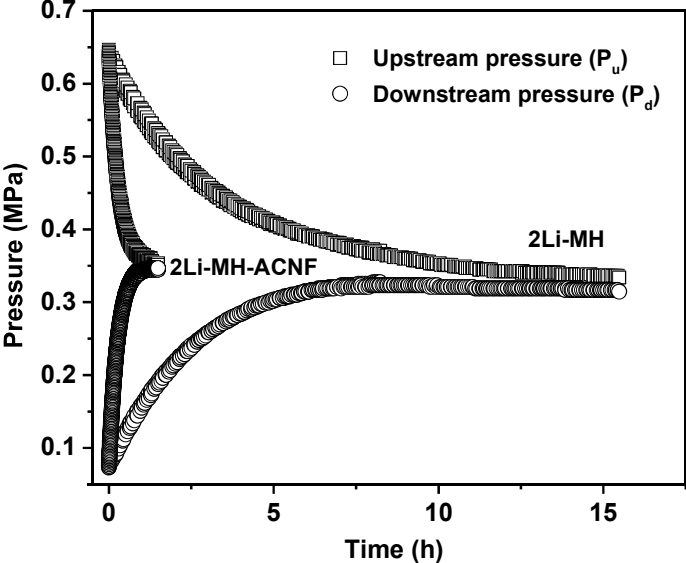


Figure 5

Figure 6

(A)



(B)

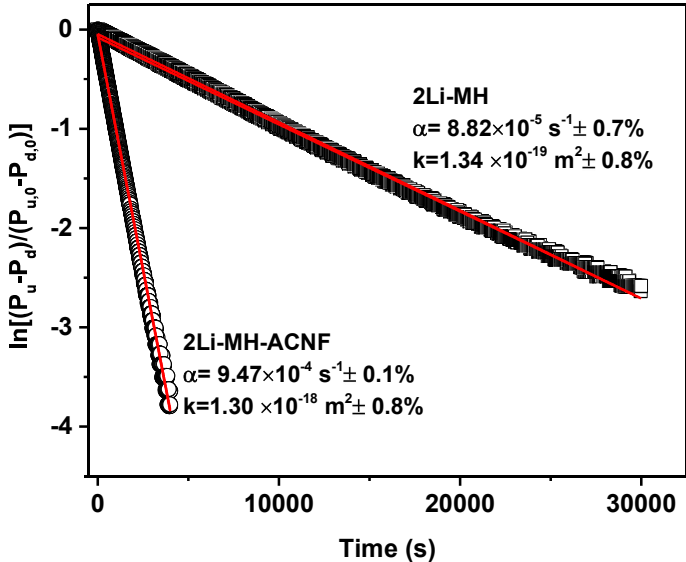


Figure 6